

Temperature-dependent chirped coherent phonon dynamics in Bi_2Te_3 using high intensity femtosecond laser pulses

N. Kamaraju, Sunil Kumar and A. K. Sood*

*Center for Ultrafast Laser Applications (CULA) and Department of Physics,
Indian Institute of Science, Bangalore - 560 012, India*

Abstract

Degenerate pump-probe reflectivity experiments have been performed on a single crystal of bismuth telluride (Bi_2Te_3) as a function of sample temperature (3K to 296K) and pump intensity using ~ 50 femtosecond laser pulses with central photon energy of 1.57 eV. The time resolved reflectivity data show two coherently generated totally symmetric A_{1g} modes at 1.85 THz and 3.6 THz at 296K which blue shift to 1.9 THz and 4.02 THz, respectively at 3K. At high photoexcited carrier density of $\sim 1.7 \times 10^{21}\text{cm}^{-3}$, the phonon mode at 4.02 THz is two orders of magnitude higher positively chirped (i.e the phonon time period decreases with increasing delay time between the pump and the probe pulses) than the lower frequency mode at 1.9 THz. The chirp parameter, β is shown to be inversely varying with temperature. The time evolution of these modes is studied using continuous wavelet transform of the time-resolved reflectivity data.

PACS numbers:

* Electronic mail: asood@physics.iisc.ernet.in

INTRODUCTION

When a narrow band gap semiconductor is excited with intense femtosecond laser pulses, a dense electron-hole plasma is produced due to the promotion of electrons from bonding states to anti-bonding states, which can cause large changes in bond lengths leading to possible structural transitions [1, 2]. The photo-excitation of carriers changes the equilibrium positions of the atoms; the atoms then oscillate around their new equilibrium positions, a mechanism called as displacive excitation of coherent phonons (DECP) [3–5]. Thus, DECP is the dominant mechanism in opaque samples [3] compared to impulsive stimulated Raman scattering (ISRS) [6] in transparent materials. Later, it was shown that DECP is a special case of ISRS when excited resonantly [7]. The investigations of coherent phonons performed under high photo-excited carrier density (PCD) $> 10^{20} \text{ cm}^{-3}$ have been very few till now [8–14].

In tellurium, time resolved reflectivity experiments [8] performed using 100 fs pulses at a PCD of $\sim 5 \times 10^{21} \text{ cm}^{-3}$ showed an instantaneous large red shift (13%) of A_1 coherent phonon frequency, attributed to the electronic softening or bond weakening [15]. In addition, the phonon time period decreasing with the delay time between the pump and probe pulses corresponds to an asymmetric line shape in frequency domain. This linear sweep in the frequency with the pump-probe time delay, termed as phonon chirping, originates from the rapid change of photoexcited carrier density across the sample thickness due to carrier diffusion resulting in different amounts of phonon renormalization [10]. In case of a semimetal, bismuth [12, 13] at carrier density of $\sim 3 \times 10^{21} \text{ cm}^{-3}$ in a degenerate pump-probe reflectivity experiment done at room temperature, A_{1g} coherent phonons were also found to be positively chirped with large oscillation amplitudes of $\sim 0.13 \text{ \AA}$ [12]. Further, collapse and revival of chirped coherent phonon oscillations were observed in the reflectivity data when the carrier density was increased further beyond a critical carrier density levels ($3.5 \times 10^{21} \text{ cm}^{-3}$ at 10K and $5 \times 10^{21} \text{ cm}^{-3}$ at 296K) [13]. This behavior was explained in terms of dynamics of a phonon wave packet in an anharmonic potential, where the packet periodically breaks up and revives to its original form, implying a nonclassical dynamics. A detailed first principle density functional calculations and optical double pump pulse experiments show that the anharmonic contribution to the phonon period is negligible under such high pump fluence regime in bismuth [14] and tellurium [8, 10] and time dependence of carrier plasma

density alone is able to explain the observed softening of the phonons.

Now, we turn to Bi_2Te_3 -subject matter of the present study. Bi_2Te_3 is an important material both from the point of view of thermoelectric [16] as well as exotic physics of topological insulators [17, 18]. There have been two earlier studies [19, 20] of Bi_2Te_3 using non-degenerate pump probe experiments at room temperature with 100 fs pulses where pump fluence was kept below $1 \text{ mJ}/\text{cm}^2$. In ref [19], the two observed coherent phonon modes at 1.85 THz and 3.68 THz were assigned as A_{1g} and its second harmonic. In a later study [20], the modes seen at 1.85 THz and 4.02 THz were assigned to two allowed A_{1g} modes, in agreement with conventional Raman measurements [21]. The objective of the present work is to study coherent phonons in single crystal of Bi_2Te_3 as a function of temperature (from 296 K to 3 K) at high photoexcited carrier densities, with a view (i) to understand the assignment of the high frequency coherent mode (first order *vis a vis* second order) and (ii) to study phonon chirping. The Gabor wavelet transform has been performed on time domain data to study the evolution of the coherent phonon modes. We note that earlier studies on Bi_2Te_3 [19, 20] were done only at room temperature and low pump fluences (with negligible chirping).

EXPERIMENTAL DETAILS

A single crystal of Bi_2Te_3 ($6 \times 6 \times 0.5 \text{ mm}^3$) with a cleaved surface perpendicular to the trigonal axis mounted on a continuous helium flow cryostat was used in our experiments. Femtosecond pulses were derived from Ti:Sapphire amplifier (Spitfire, Spectra Physics Inc) producing ~ 50 fs pulses with the central photon energy of 1.57 eV at a repetition rate of 1 KHz. The pump beam was modulated at 393 Hz with a chopper and the reflected probe intensity was recorded using a Si-PIN diode and a lock-in amplifier. The spot size (half width at $1/e$ maximum) of the pump and probe beams were kept at $\sim 600 \mu\text{m}$ and $400 \mu\text{m}$, respectively at the overlap of the two beams on the sample. The pulse width was measured to be 65 fs (full width at half maximum) using a thin beta-barium borate (BBO) crystal at the sample point. The polarization of the pump beam was kept perpendicular to that of the probe beam to avoid scattered pump light reaching the detector. Both the pump and probe beams were kept close to normal incidence. The crystal surface is seen to get damaged at pump fluence beyond $\sim 4.5 \text{ mJ}/\text{cm}^2$ and hence all our experiments were done

at pump fluences of 3.3 mJ/cm² and 1.3 mJ/cm², whereas the probe fluence was kept at 0.4 mJ/cm². The time resolved reflectivity of the sample was recorded as a function of sample temperature varying from 296K to 3K.

Bi₂Te₃ is a narrow band semiconductor with an indirect band gap of 0.15 eV and it crystallizes in the R $\bar{3}m$ structure with the point group D_{3d}⁵. It is made up of close-packed atomic layers which are periodically arranged along the c-axis in five layers (Te⁽¹⁾-Bi-Te⁽²⁾-Bi-Te⁽¹⁾) called as ‘quintuples’. These layers are bonded by van der Waals force and the weakest link among the layers is Te⁽¹⁾-Te⁽¹⁾. Five atoms per hexagonal unit cell ($a = 4.38 \text{ \AA}$, $c = 30.49 \text{ \AA}$) give totally twelve optical phonons out of which four are Raman active modes [21, 22] represented as 2 A_{1g}(observed at 1.86 THz and 4.02 THz) + 2 E_g (observed at 1.1 THz and 3.09 THz). The linear absorption coefficient, α of Bi₂Te₃ at 1.57eV is $\sim 4 \times 10^5 \text{ cm}^{-1}$ [23] and thus the penetration depth, ξ ($\sim 1/\alpha$) is 25 nm. This corresponds to PCD, N_0 ($\equiv 6.25 \times 10^{18} F\alpha(1 - R)/E_p$) $\sim 1.7 \times 10^{21} \text{ cm}^{-3}$ at pump fluence $F = 3.3 \text{ mJ/cm}^2$ at the sample surface, which is about 1% of all the valence electrons. Here R=0.68 is the reflectivity coefficient of Bi₂Te₃, at photon energy E_p of 1.57 eV.

RESULTS AND DISCUSSION

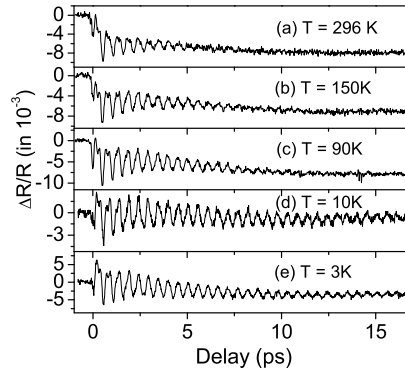


FIG. 1: Normalized time resolved reflectivity change ($\Delta R/R$) of bismuth telluride as the function of the time delay between the pump and probe pulses at various temperatures (a) T = 296 K, (b) 150 K, (c) 90 K, (d) 10 K, (e) 3 K (colour online).

The coherent phonon mode’s normal coordinate is written as [24], $Q = b \exp(-\pi\gamma t) \cos(2\pi\nu_0 t + \phi)$ where b , γ , ν_0 and ϕ are the amplitude, damping constant, fre-

quency and the initial phase of the coherent phonon mode. To first order in Q , the normalized change in reflectivity ($\Delta R/R$) of a probe beam due to generation of two A_{1g} coherent phonon modes ($A_{1g}^{(1)}$ and $A_{1g}^{(2)}$) in an absorptive material can be written as

$$\frac{\Delta R}{R} = \sum_{i=1,2} \left[\frac{\partial(\Delta R/R)}{\partial Q} \right] b_i \exp(-\pi\gamma_i t) \cos(2\pi\nu_i t + \phi_i) \quad (1)$$

Here $i = 1$ and 2 corresponds to $A_{1g}^{(1)}$ and $A_{1g}^{(2)}$ respectively. The time resolved reflectivity data for Bi_2Te_3 at a few temperatures using pump fluence of 3.3 mJ/cm^2 are shown in Fig. 1. The signal contains both non-oscillatory and oscillatory components. The non-oscillatory background arising from carrier dynamics was removed by a digital band pass filter to extract the oscillatory part [19, 20]. The oscillatory part of the transient normalized differential reflectivity data was analyzed using Eq. (1). The fit was satisfactory at room temperature but was not good at lower temperatures. This necessitated the inclusion of chirp parameter β in Eq. (1) as [13]

$$\frac{\Delta R}{R} = \sum_{i=1,2} B_i \exp(-\pi\gamma_i t) \cos(2\pi\nu_i t + \beta_i t^2 + \phi_i) \quad (2)$$

where $B_i = \left[\frac{\partial(\Delta R/R)}{\partial Q} \right] b_i$ is the coherent phonon amplitude and β_i is the chirp parameter. This fit was found to be excellent over the entire temperature range. For example, Fig. 2(a) displays the digital band pass filtered time domain data at 3K recorded using pump fluence of 3.3 mJ/cm^2 along with the fit using Eq. (1) (dashed line) and (2) (solid line), and Fig. 2 (b) shows the corresponding fast Fourier transform (FFT) of the data and the fits. Here the FFT intensity of the second mode in the frequency range of 3 THz - 5 THz is appropriately scaled up to compare with the first mode. The eigen vectors corresponding to the A_{1g} modes [21] are also shown as the inset of Fig. 2(b). It may be very difficult to see the chirping effect in time domain as the higher frequency mode is very short lived (1.2 ps) and therefore, frequency domain is a better choice in identifying the chirp in such cases. The FFT of the fitted function in time domain (Eq. (2)) with chirp ($\beta \neq 0$) shown by continuous line) fits the FFT of the measured data (open circles) much better than without β , i.e $\beta = 0$ (short dashed line)[Fig. 2(b)]. The value of $\beta_2 = 0.38\text{ps}^{-2}$ is much higher than $\beta_1(\sim 2 \times 10^{-3} \text{ ps}^{-2})$. When the pump fluence is decreased to 1.3 mJ/cm^2 , $\beta_2 = 0.045 \text{ ps}^{-2}$ which clearly indicates that the chirping is mainly due to large number of photoexcited carriers. Since our focus is mainly on the high density photo carriers mediated coherent

phonons, the temperature dependence of the fit parameters at highest pump fluence of 3.3 mJ/cm² are discussed from here on.

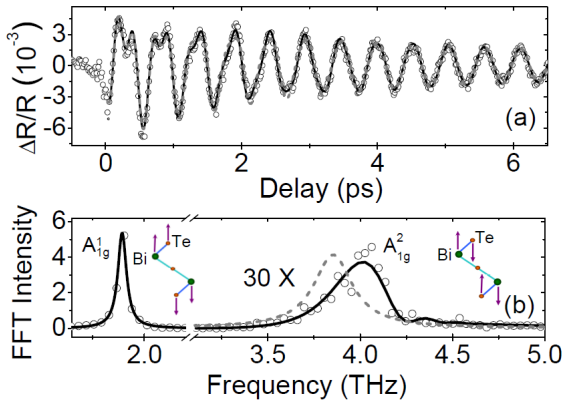


FIG. 2: (a) Digital band pass filtered normalized time resolved differential reflectivity data at $T = 3\text{K}$ (open circles) along with their fits according to Eq. (1) (dashed line) and (2) (solid line). (b) The corresponding FFT of the time domain data and the fits. The data in the range of 3 THz -5 THz has been scaled appropriately to compare the asymmetry seen at 3K. Here, the short dashed line is the FFT of the fit without chirp parameter. The eigen vector of the two A_{1g} modes are shown in the FFT panel (colour online).

The parameters (filled diamond) obtained from the fit of the time domain data are plotted as a function of temperature in Fig. 3. Though the dependence of β_1 and β_2 on temperature are similar, the chirp parameter β_2 for the high frequency $A_{1g}^{(2)}$ phonon mode is almost two orders higher compared to β_1 showing that electron-phonon interaction for $A_{1g}^{(2)}$ should be much higher than that for $A_{1g}^{(1)}$ (Figs. 3(a) and (b)). The increased phonon chirping seen at low temperatures and its inverse dependence on temperature $\beta \sim T^{-1}$ is shown using continuous lines. An increase of β with decreasing temperature can be qualitatively understood by considering the carrier diffusion across the penetration depth of ξ in Bi_2Te_3 . At very high carrier densities ($\sim 10^{21}$), it has been shown that the carrier diffusion coefficient, D_a has major contributions from carrier-carrier scattering mediated diffusion, D_{eh} [25, 26]. In such a case $D_a \sim T^{5/2}$ and hence the diffusion time $\tau_{\text{diff}} \equiv \xi^2/D_a \sim T^{-5/2}$. This inverse power law dependence suggests that at low temperatures, the diffusion time is longer and hence electron phonon interaction will result in large chirping. The temperature dependence of chirping as $\beta \sim T^{-1}$ needs new theoretical inputs.

Next, we turn to the phonon amplitudes. It is seen that both the coherent phonon amplitudes, B_1 and B_2 increase as the temperature is lowered (Figs. 3.(c) and (d)). It has been shown [27] that the coherent phonon amplitude, B_{ph} behaves quite similar to the temperature dependence of the Raman peak intensity [27] since the source of spontaneous Raman scattering and the driving force in the generation of coherent phonons through ISRS are the same [28]. The Raman cross-section increases with temperature as $[n(\nu) + 1]$ (where $n(\nu)$ is the Bose-Einstein statistical factor) and hence the Raman peak intensity can be written as, $I_p \sim \frac{[n(\nu)+1]}{[2n(\nu/2)+1]}$, where the temperature dependence in the denominator comes from the cubic anharmonic contributions to the linewidth. The fit (solid line) using this expression is shown along with the data for B_1 and B_2 in Fig. 3(c) and (d).

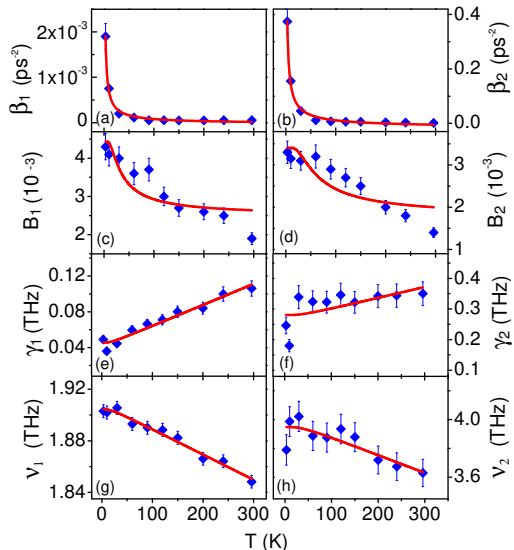


FIG. 3: Phonon chirp parameters [(a) and (b)], amplitude of oscillations [(c) and (d)], damping constant [(e) and (f)] and frequency [(g) and (h)] of both the coherent A_{1g} modes obtained from time domain fit to the data with high pump intensity (Filled diamonds) versus sample temperature. The continuous lines in (a)-(h) are the fits (see text) (colour online).

The temperature dependence of coherent phonon damping factor and the frequency of the two modes are displayed in Fig. 3(e),(g) and Fig. 3(f),(h), respectively. In the case of $A_{1g}^{(1)}$, the frequency decreases from 1.9 THz to 1.84 THz, i.e., a decrease of 3% as the crystal is heated from 3K to 296K and the damping term increases by 150 % from ~ 0.04 THz at 3K to ~ 0.1 THz at 296K. The behavior of the second mode is rather interesting: the

damping constant becomes almost constant after 60K and the frequency decreases from 4.0 THz to 3.6 THz (10% change) when the crystal temperature increases from 3K to 296K. The fit (thick line) shown in the figure is by using the well known functions [29] based on cubic anharmonicity where the phonon of frequency, ν decays into two phonons of equal frequency: $\gamma_{ph}(T) = \gamma_0 + C[1 + 2n(\nu_0/2)]$ and $\nu_{ph}(T) = \nu_0 + A[1 + 2n(\nu_0/2)]$ where ν_0 (frequency at T=0K), A, C and γ_0 (disorder induced damping) are the fitting parameters (A and C are the measures of third order cubic anharmonicity). The parameters obtained from fitting are, $\nu_0 = 1.908$ THz, A = -0.005 THz, $\gamma_0 = 0.040$ THz and C = 0.005 THz for $A_{1g}^{(1)}$ mode; and $\nu_0 = 4.007$ THz, A = -0.060 THz, $\gamma_0 = 0.263$ THz and C = 0.017 THz for $A_{1g}^{(2)}$ mode. Thus the disorder induced damping (γ_0) and anharmonicity (A and C) are more for $A_{1g}^{(2)}$ compared to $A_{1g}^{(1)}$. It can be seen from Fig. 3(h) that the temperature dependence of ν_2 is non-monotonic. The decrease of ν_2 at 3K may be due to the chirp in the frequency whose quantitative understanding is lacking.

Finally, to examine whether the second mode at ~ 4 THz is the second harmonic of the first A_{1g} mode at 1.8 THz as suggested in ref [19], we re-fitted the digitally band pass filtered time domain data with $\frac{\Delta R}{R}$ expressed in a second order approximation in Q as [19]

$$\frac{\Delta R}{R} = \left[\frac{\partial(\Delta R/R)}{\partial Q} \right] Q + \frac{1}{2} \left[\frac{\partial^2(\Delta R/R)}{\partial Q^2} \right] Q^2 \quad (3)$$

where Q is for the $A_{1g}^{(1)}$ phonon mode. Taking the expression for Q as in Eq. (1) (since β_1 is small), the fit according to Eq. (3) was unsatisfactory as the second mode could never be accommodated in the fit to the data as shown in Fig. 4. In Fig. 4, the time domain data (thin line) along with the new fit (thick line) using Eq. (3) and their FFT are shown in (a)-(b) for 3K and in (c)-(d) for 296K where open circles are the FFT of the data and thick lines are the FFT of the fit. It can be seen from these figures that the fit is not compatible with the data in both frequency and time domain. At 296K, though the fit seemingly agrees with the data in the frequency domain, it is not so in time domain. This confirms that the higher energy phonon mode is not a second order mode of $A_{1g}^{(1)}$. To further elucidate this point, we have analyzed the temperature dependence of the ratio of the integrated intensities of coherent phonons, $\frac{B_2\gamma_2}{B_1\gamma_1}$ (open circles in Fig.4(e) where the y-axis is normalized to the ratio at 3K). Here, we consider two cases: (i) For ν_1 and ν_2 with $\nu_2 > \nu_1$ as the single phonon modes (SPM), the ratio of their integrated intensity, is $\sim \frac{n(\nu_2)+1}{n(\nu_1)+1}$ shown by solid line in Fig. 4(e), (ii) for ν_2 as the second harmonic or two phonon mode (TPM) of ν_1 ($\nu_2 = 2\nu_1$), we note

that the ratio of their integrated intensity is $[n(\nu_1) + 1]^2/[n(\nu_1) + 1] = n(\nu_1) + 1$ shown by dashed line in Fig. 4 (e). Thus, it is clear from Fig. 4 (e) that SPM is compatible with the data corroborating our conclusion that the high frequency mode is a single phonon mode and not a second harmonic of $A_{1g}^{(1)}$.

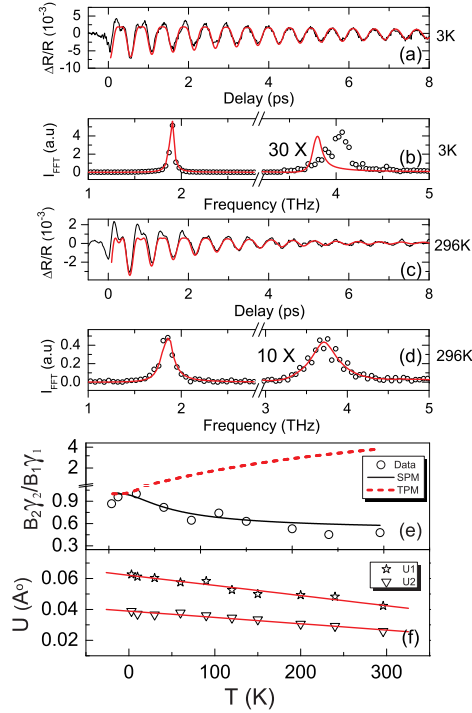


FIG. 4: The time domain data (thin line) along with the fit (thick line) according to Eq. (3) and their FFT are shown in (a)-(b) for $T=3\text{K}$ and (c)-(d) for $T=296\text{K}$. In (b) and (d), the open circles are the FFT of the data and thick line is the FFT of the fit. The ratio of integrated coherent phonon intensity (open circles), $\frac{B_2\gamma_2}{B_1\gamma_1}$ along with the fit using single phonon (SPM) (thick line) and two phonon model (TPM) (dashed line) are shown in (e). The estimated lattice displacements for the two coherent phonon modes (open star for U_1 and open inverted triangle for U_2) are given in (f) along with a linear fit (colour online).

The lattice displacement of the coherent phonon modes at 1.9 THz and 4.02 THz can be estimated for absorbing materials using [11, 30]

$$U_i^2 \sim \frac{3.8 \times 10^{-3} B_i F}{\rho\nu_i|\varepsilon|} \left[\frac{\left(\frac{2\varepsilon_2}{E_{ph}}\right)}{D} \right] \quad (4)$$

where U_i is in Angstrom (\AA), F is the pump fluence in mJ/cm^2 , ρ is the density of the material in $\text{amu}/\text{\AA}^3$ and ε is the dielectric constant ($\varepsilon_1 + j\varepsilon_2$), E_{ph} is the energy of the phonon in eV and $D = \frac{1}{R} \frac{\partial R}{\partial E}$ with E as the photon energy in eV. Now, for Bi_2Te_3 , $D = \frac{1}{R} \frac{\partial R}{\partial E} \sim 10^{-1} \text{eV}^{-1}$ at 1.57 eV and $\frac{2\varepsilon_2}{E_{ph}} \sim 10^3 \text{eV}^{-1}$ with $\varepsilon = 2.75 + j 15$ at 1.57 eV [23]. Thus, for Bi_2Te_3 , the lattice displacement is

$$U_i \sim \sqrt{B_i \frac{38 F}{\rho \nu_i |\varepsilon|}} \quad (5)$$

The temperature dependence of U_1 and U_2 thus estimated is shown in Fig. 4 (f), which essentially arises from temperature dependence of B_i and ν_i . A linear fit (line) to U is shown in the figure.

To capture the evolution of coherent phonons with time, we have performed continuous wavelet transform (CWT) similar to that used by Hase et al. [31] in observing the birth of a quasiparticle in silicon. We have used the MATLAB code [32] modified for Gabor mother wavelet based on Gaussian function given as [33],

$$\Psi(t/s) = \pi^{-1/4} \left(\frac{1}{ps} \right)^{1/2} \exp \left[-\frac{t^2}{2s^2p^2} + j \frac{t}{s} \right] \quad (6)$$

where s is the scaling factor (inverse of frequency) and $p = \pi(2/\ln(2))^{1/2}$ is a constant. Here, we describe the procedure to calculate the continuous wavelet transform. The wavelet transform of a given time signal, $x(t)$ is given by,

$$CWT(\tau, s) = \frac{1}{\sqrt{|s|}} \int x(t) \Psi^*((t - \tau)/s) dt \quad (7)$$

A starting scale, s_{start} corresponding to a frequency higher than the highest frequency of the signal (determined by FFT) is chosen and the starting wavelet $\Psi_{start}(t/s_{start})$ in time domain here is a compressed wavelet. The cross correlation of $\Psi_{start}(t)$ with $x(t)$ is computed using Eq. (7) with $\tau = 0$. The magnitude of cross correlation will depend on how closely the frequency components in $x(t)$ and $\Psi_{start}(t)$ match. This procedure is repeated by translating $\Psi_{start}(t)$ in time domain (τ) and this gives wavelet coefficients for a given s and a range of values of τ . The whole procedure is again repeated for next higher s . Thus, one gets a range of wavelet coefficients of $x(t)$ in time-scale plane which is then converted into time-frequency plane. The wavelet transform of a time domain signal gives three dimensional (3D) plot of wavelet coefficients vs frequency and time. CWT chronograms (contour of the 3D plot) of

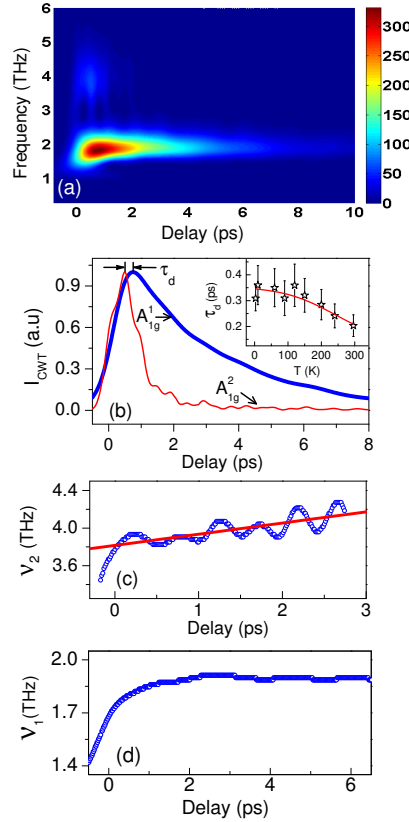


FIG. 5: (a) CWT chronogram of high pump intensity data at $T=3\text{K}$. The color bars are given at the right side to symbolically represent the CWT intensity. (b) The maximum of CWT intensity at each time delay for both modes (thicker line is for $A_{1g}^{(1)}$ mode and the thinner line is for the $A_{1g}^{(2)}$ mode). The time delay between the two modes (open stars) are plotted as a function of sample temperature in the inset where the thick line is the guide to the eye. (c) The frequency corresponding to the maxima of CWT intensity at each time delay for $A_{1g}^{(2)}$ (thicker line is the linear fit to the data) and for (d) $A_{1g}^{(1)}$ mode. (see text) (color online).

the time domain data at 3K and high pump excitation ($3.3 \text{ mJ}/\text{cm}^2$), are shown in Fig 5 (a). It can be seen from Fig 5 (a) that at 3K, the frequency of $A_{1g}^{(1)}$ mode starts at 1.5 THz and reaches 1.9 THz in $\sim 750 \text{ fs}$ and this time is seen to be constant at all the temperatures. We could not resolve a similar build up in frequency for the $A_{1g}^{(2)}$ due to its short lifetime (0.9-1.6 ps) compared to the first mode (4-10 ps). To get more insight into these chronograms, the maximum of CWT intensity at each time delay (time slice) was calculated and plotted at 3K for both the modes (Fig. 5(b)). Here, thicker line is for $A_{1g}^{(1)}$ and the thinner line is for

$A_{2g}^{(2)}$. The time to reach the maximum of CWT is $\sim 750 \pm 20$ fs for A_{1g}^1 mode and $\sim 510 \pm 20$ fs for A_{1g}^2 mode. The time delay of $\sim 240 \pm 20$ fs between the maxima of the two modes A_{1g}^1 and A_{1g}^2 is found to be dependent on the sample temperature as shown in the inset of Fig. 5 (b). The reason for the time delay and its temperature dependence is yet to be understood. The phonon chirp for the second mode is demonstrated through the plot of frequency (open circles) corresponding to the maxima of CWT intensity at each time delay at 3K in Fig. 5 (c). Thicker line is the linear fit to the data with $\nu_2(\text{THz}) = 3.8 + \beta_2/(2\pi)t$ where t is the time delay in ps. This corresponds to $\beta_2 = 0.41 \text{ ps}^{-2}$, closely matching to the value of 0.38 ps^{-2} derived from the time domain fit. The oscillatory structures seen in the frequency is an artifact in the wavelet transform when the separation between the two frequencies is less than 4 THz. Similar analysis for A_{1g}^1 mode is given in Fig. 5 (d) where the build-up time is ~ 750 fs (consistent with Fig. 5 (b)) and the frequency is seen to be constant with delay time as expected since β_1 is very small. We note that the above analysis using AGU-Vallen-wavelet [34] resulted in similar results.

CONCLUSIONS

In conclusion, we have studied coherent A_{1g} phonons in Bi_2Te_3 as a function of both temperature and pump fluence. We have observed that the higher frequency coherent phonon mode at ~ 4.0 THz is $A_{1g}^{(2)}$ and is not a second harmonic of $A_{1g}^{(1)}$. It acquires two orders of magnitude higher positive chirping at the lowest temperatures and high pump fluence as compared to the $A_{1g}^{(1)}$ phonon. The chirp in time domain is manifested as an asymmetry in the frequency domain. The wavelet transform of the time domain differential reflectivity helps to identify the chirp and the time for a phonon mode to build up to its maximum amplitude. We hope our experiments will motivate theoretical calculations to understand the exact temperature dependence of phonon chirping at highly excited carrier densities, higher chirping for $A_{1g}^{(2)}$ and the different build up times for two coherent modes.

AKS acknowledges the financial support from Department of Science and Technology of India and CSIR for the Bhatnagar Fellowship. SK acknowledges University Grants Commission, India for senior research fellowship.

-
- [1] L. Huang, J. P. Callan, E. N. Glezer, and E. Mazur, Phys. Rev. Lett. **80**, 185 (1998).
- [2] C. W. Siders, A. Cavalleri, K. S-Tinten, Cs. Tóth, T. Guo, M. Kammler, M. H. v. Hoegen, K. R. Wilson, D. von der Linde, C. P. J. Barty, Science 286, 1340 (1999).
- [3] H. J. Zeiger, J. Vidal, T. K. Cheng, E. P. Ippen, G. Dresselhaus, M. S. Dresselhaus, Phys. Rev. B. **45** 768 (1992).
- [4] T. K. Cheng, M. S. Dresselhaus, and E. P. Ippen, Appl. Phys. Lett. **62**, 1901 (1993).
- [5] A. V. Kuznetsov and C. J. Stanton, Phys. Rev. Lett. **73**, 3243 (1994).
- [6] L. Dhar, J. A. Rogers and K. A. Nelson, Chem. Rev. **94**, 157 (1994).
- [7] G. A. Garret, T. F. Albrecht, J. F. Whitaker, and R. Merlin, Phys. Rev. Lett. **77**, 3661 (1996).
- [8] S. Hunsche, K. Wienecke, T. Dekorsy, and H. Kurz, Phys. Rev. Lett. **75**, 1815 (1995).
- [9] S. Hunsche, K. Wienecke, and H. Kurz, Appl. Phys. A **62**, 499 (1996).
- [10] P. Tangney, S. Fahy, Phys. Rev. B **65**, 054302 (2002).
- [11] M. F. DeCamp, D. A. Reis, P. H. Bucksbaum, and R. Merlin, Phys. Rev. B **64**, 092301 (2001).
- [12] M. Hase, M. Kitajima, S. Nakashima, and M. Mizoguchi, Phys. Rev. Lett. **88**, 067401 (2002).
- [13] O. V. Misochko, M. Hase, K. Ishioka, and M. Kitajima, Phys. Rev. Lett. **92**, 197401 (2004).
- [14] E. D. Murray, D. M. Fritz, J. K. Wahlstrand, S. Fahy, and D. A. Reis, Phys. Rev. B **72**, 060301 (2005).
- [15] P. Stampfli and K. H. Bennemann, Phys. Rev. B **42**, 7163 (1990); **46**, 10686 (1992); **49**, 7299 (1994).
- [16] G. S. Nolas, J. Sharp, and H. J. Goldsmid, **Thermoelectrics** (Springer: New York, 2001)
- [17] C. L. Kane and E. J. Mele, Science, **314**, 1692 (2006).
- [18] J. E. Moore, Nature **464**, 194 (March 2010).
- [19] A. Q. Wu, X. Xu, and R. Venkatasubramanian, Appl. Phys. Lett. **92**, 011108 (2008).
- [20] Y. Wang, X. Xu, and R. Venkatasubramanian, Appl. Phys. Lett. **93**, 113114 (2008).
- [21] W. Richter, H. Kohler, and C. R. Becker, Phys. Stat. Sol. (b) **84**, 619 (1977).
- [22] W. Kullmann, J. Geurts, W. Richter, N. Lehner, H. Rauh, U. Steigenberger, G. Eichhorn, and R. Geick, Phys. Stat. Sol. (b) **125**, 131 (1984).
- [23] D. L. Greenaway and G. Harbeke, J. Phys. Chem. Solids **26**, 1585 (1965).
- [24] A. V. Bragas, C. Aku-Leh, S. Costantino, A. Ingale, J. Zhao and R. Merlin, Phys. Rev. B **69**,

- 205306 (2004).
- [25] N. H. Fletcher, Proc. Inst. Rad. Eng. **45**, 862 (1957).
- [26] C. -M. Li, T. Sjodin, and H. -L. Dai, Phys. Rev. B **56**, 15 252 (1997).
- [27] O. V. Misochko, K. Ishioka, M. Hase and M. Kitajima, J. Phys.:Condens. Matter **18**, 10571 (2006).
- [28] R. Merlin, Solid State Commun. **102**, 207 (1997).
- [29] M. Balkanski, R. F. Wallis, E. Haro, Phys. Rev. B **28**, 1928 (1983).
- [30] See Eq. A.22 to A.24 of M. F. Decamp, Ph.D Thesis, The University of Michigan, Ann Arbor (2002), available at <http://www.aps.anl.gov/Sectors/Sector7/Science/Publications/theses.html>. Note that in Eq. A.22, there is a typographical error in the exponent of $(\frac{2i\varepsilon_2}{E_{ph}})$ which should be 1 instead of 2.
- [31] M. Hase, M. Kitajima, A. M. Constantinescu, and H. Petek, Nature **426**, 51 (2003).
- [32] Wavelet software, <http://paos.colorado.edu/research/wavelets/software.html>
- [33] H. Suzuki, T. Kinjo, Y. Hayashi, M. Takemoto, K. Ono, J. Acoustic Emission **14**, 69 (1996).
- [34] AGU-Vallen Wavelet, <http://www.vallen.de/wavelet/index.html>